GEOPHYSICS, VOL. 76, NO. 1 (JANUARY-FEBRUARY 2011); P. S29–S39, 12 FIGS.
10.1190/1.3533914

# An effective imaging condition for reverse-time migration using wavefield decomposition

Faqi Liu[1], Guanquan Zhang[2], Scott A. Morton[1], and Jacques P. Leveille[3]

## ABSTRACT

Reverse-time migration (RTM) exhibits great superiority over other imaging algorithms in handling steeply dipping structures and complicated velocity models. However, low-frequency, high-amplitude noises commonly seen in a typical RTM image have been one of the major concerns because they can seriously contaminate the signals in the image if they are not handled properly. We propose a new imaging condition to effectively and efficiently eliminate these specific noises from the image. The method works by first decomposing the source and receiver wavefields to their one-way propagation components, followed by applying a correlation-based imaging condition to the appropriate combinations of the decomposed wavefields. We first give the physical explanation of the principle of such noises in the conventional RTM image. Then we provide the detailed mathematical theory for the new imaging condition. Finally, we propose an efficient scheme for its numerical implementation. It replaces the computationally intensive decomposition with the cost-effective Hilbert transform, which significantly improves the efficiency of the imaging condition. Applications to various synthetic and real data sets demonstrate that this new imaging condition can effectively remove the undesired low-frequency noises in the image.

## INTRODUCTION

Depth migration algorithms are broadly categorized as ray-based and wave equation-based methods. Each group can be further divided into subclasses: the ray-based methods include Kirchhoff and beam migrations, whereas the wave-equation group consists of one-way wave equation-based migration and the full acoustic wave equation-based reverse-time migration (RTM). The ray-based Kirchhoff method was the dominant imaging algorithm in the oil and gas industry in the late 1990s. This method can image steeply dipping structures and overhangs. It is efficient, flexible, and can be used in a target-oriented fashion. However, because rays are asymptotic solutions to the wave equation, Kirchhoff methods are not effective in imaging complicated structures, especially because the typical implementation is limited only to a single arrival. Beam migration has the same advantages as Kirchhoff migration in that it can properly handle steeply dipping structures and is also a target-oriented scheme. It has an advantage over Kirchhoff migration in that it is inherently multiarrival. However, beam migration is still fundamentally a ray-based, asymptotic method and fails to function properly in complicated velocity models.

One-way wave equation-based migration methods utilize the paraxial approximation to the wave equation to extrapolate the wavefields from one depth to another for each frequency component. These methods work well for waves propagating in directions within certain angle limits from the main direction (usually the vertical direction), but they fail to handle waves propagating at wider angles, especially those near or beyond 90°. Thus, a typical one-way wave equation-based migration method cannot image steeply dipping reflectors. Most of these methods differ in the way they approximate the acoustic wave equation and the maximum dip angles that they can properly represent (Etgen et al., 2009).

On the other hand, RTM directly solves the full (two-way) acoustic wave equation for wavefield propagation, and for that reason, it has proven to be the preferred imaging algorithm in many geologically complex basins of the world, such as the Gulf of Mexico. Its superiority becomes more important as our exploration for hydrocarbons encounters more and more challenging geological settings, such as structures with steep dips or overhangs, which are beyond the limits of one-way wave equation-based migration algorithms. Nevertheless, complex structures are often accompanied by strong lateral velocity variations, which result in significant multipathing,

Manuscript received by the Editor 23 April 2010; revised manuscript received 15 July 2010; published online 14 January 2011; corrected version published online 18 January 2011.
[1]Geoscience Technology, Hess Corporation, Houston, TX. E-mail: FLiu@Hess.com; Morton@Hess.com.
[2]State Key Laboratory of Scientific/Engineering Computing, Academy of Mathematics and System Sciences, Chinese Academy of Sciences, Beijing, People's Republic of China. E-mail: zgq@LSEC.cc.ac.cn.
[3]Formerly Geoscience Technology, Hess Corporation, Houston, TX; presently at ION Geophysical, Houston, TX. E-mail: jacques.leveille@iongeo.com.

limiting the effectiveness of ray-based Kirchhoff migration. Even the beam migration methods often become ineffective in such areas. RTM outperforms all of these methods in imaging such complicated structures.

RTM was initially investigated in the early 1980s (Baysal et al., 1983; Loewenthal and Mufti, 1983; McMechan, 1983; Whitmore, 1983). However, it has only recently been widely applied in a production mode because of its extensive computational cost. This method requires extrapolating the source and receiver wavefields in time, followed by applying an appropriate imaging condition to construct the image. The image in RTM is traditionally constructed by taking the zero-lag crosscorrelation of the extrapolated source and receiver wavefields. This imaging condition provides the correct kinematics and is extremely simple to implement (Claerbout, 1985). However, it often produces a significant amount of large-amplitude, low-frequency noise at sharp interfaces that contaminate the image (for example, see Figures 1–3). This has been one of the major concerns in RTM, and substantial effort has been devoted to its attenuation. Although this imaging condition is not unique to RTM, it is widely used in one-way wave-equation migration. However, these noises only exist in RTM results. Such noises result from the unwanted crosscorrelation of the source and receiver wavefields at nonreflecting points along a raypath.

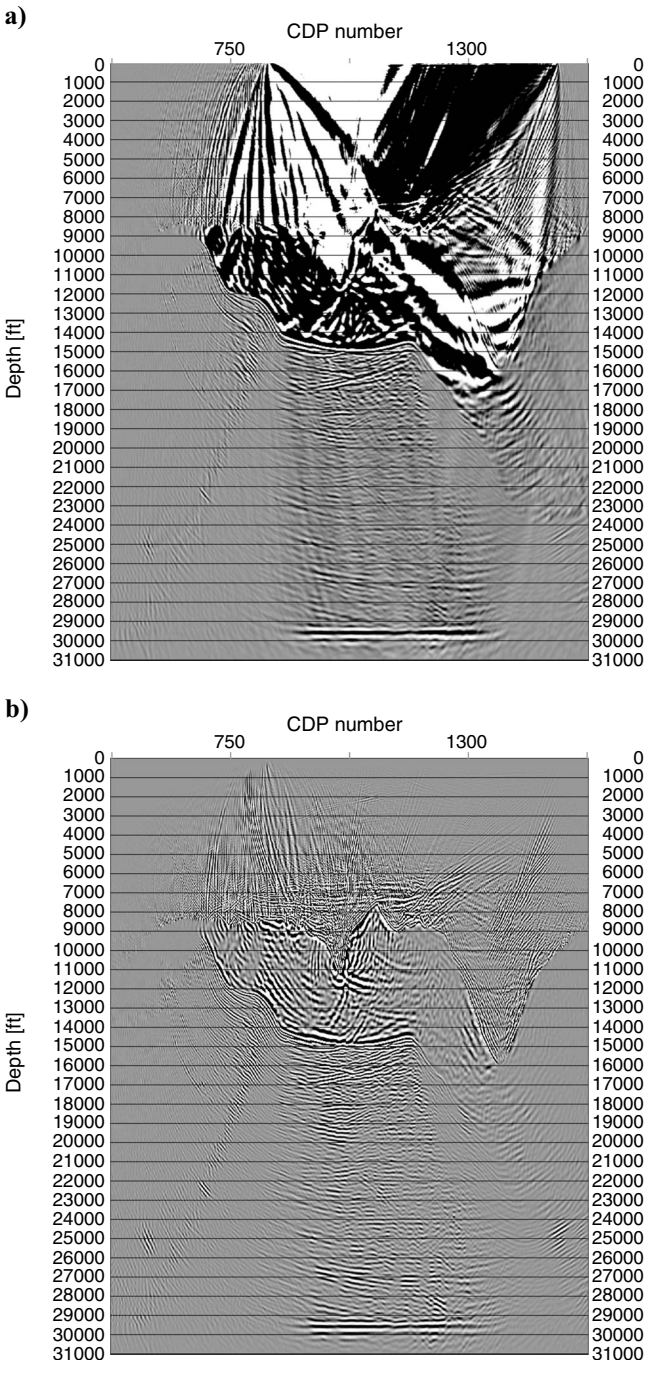


Figure 1. (a) Reverse-time migration of one shot gather in the 2D Sigsbee model using the crosscorrelation imaging condition. (b) Band-pass filtered result of the image in panel a.

In poststack RTM, reflections at interfaces can be suppressed by artificially matching the impedance of the media at the two sides of an interface, which results in the nonreflecting wave equation (Baysal et al., 1984). Another effective approach is to smooth the velocity model to reduce the reflections (Loewenthal et al., 1987). However, both approaches become less effective in prestack cases because reflections can still occur at non-zero incident angles at a velocity interface when the impedances are the same. Those noises must therefore be eliminated by a different imaging condition. Fletcher et al. (2005) proposed to remove the imaging noise by applying a directional damping factor. Yoon and Marfurt (2006) proposed using the Poynting vector to improve the crosscorrelation-based imaging condition. Guitton et al. (2006) tried to remove the artifact using a least-square filter; Zhang and Sun (2009) proposed two approaches to attenuate the artifacts: One works by muting the prestack angle gathers, and the other involves scaling the input data and filtering the stacked image using a Laplacian filter.

This paper expands our previous work (Liu et al., 2007). We first investigate in detail the physics that creates these noises in RTM. We then propose a correlation-based imaging condition to eliminate the noises. The new imaging condition first needs to decompose the full wavefields into their one-way components along a certain specific direction. The correlation imaging condition is then applied to the oppositely propagating combinations of the decomposed wavefields. We also propose an efficient algorithm to implement it. We discuss the theory in detail, followed by some synthetic and field data examples to demonstrate that the new imaging condition is successful in removing the undesired artifacts.

## REVERSE-TIME MIGRATION

A prestack RTM algorithm is a three-step scheme consisting of (a) forward extrapolating the source wavefield; (b) backward extrapolating the receiver wavefield, both in time; and (c) applying a proper imaging condition to construct an image where a reflection occurred. At the present time, this algorithm has largely been limited to the simplified constant density acoustic case, which is characterized by the wavefields propagated using the full acoustic wave equation

$$\frac{1}{v^2(\vec{x})}\frac{\partial^2}{\partial t^2}p(t,\vec{x}) = \nabla^2 p(t,\vec{x}), \tag{1}$$

where $p(t,\vec{x})$ is the pressure wavefield at a spatial location $\vec{x} = (x,y,z)$ and time $t$, and $v(\vec{x})$ is the sound velocity in the propagation medium.

In RTM, the source and receiver wavefields are extrapolated using equation 1. The image is conventionally constructed by taking the

zero-lag crosscorrelation of the extrapolated source and receiver wavefields defined as follows:

$$I(\vec{x}) = \int_0^{T_{\max}} s(t,\vec{x})r(t,\vec{x})dt. \quad (2)$$

Here, $s(t,\vec{x})$ is the forward extrapolated source wavefield, $r(t,\vec{x})$ is the backward propagated receiver field at spatial location $\vec{x}$ and time $t$, and $T_{\max}$ represents the maximum extrapolation time. Note that here we represent the receiver wavefield in the time of wavefield propagation rather than that for the numerical extrapolation ($T_{\max} - t$).

Equation 2 provides the correct kinematics for a reflection in which incident and reflected wavefields are coincident in space and time, and it is very efficient to implement because it only requires the two wavefields (source and receiver) at a single time step to be available at any point in the computation. However, these two fields are extrapolated in the opposite directions with respect to the time axis; that is, the source wavefield is extrapolated forward in time starting at time zero at a source location, whereas the receiver wavefield is computed backward starting at the maximum recorded time at the receivers. To make the two wavefields ready for equation 2, three general computational approaches can be seen as viable choices to handle the source wavefield: One is to save all of the forward extrapolated source wavefields to disk and read them back to memory as needed; another approach is to save the wavefields only at certain discrete time steps, and the wavefields at other intermediate time steps are then recomputed by interpolation or extrapolation (Symes, 2007); and a third option is to save the values of the wavefield only at the boundary for all of the time steps, and the wavefields at all inner grid points are recomputed using those saved values as boundary conditions. Each of these approaches has its advantages and shortcoming depending on the system configuration (Dussaud et al., 2008).

Unfortunately, the imaging condition defined in equation 2 usually generates large-amplitude noise that contaminates the image near sharp interfaces. Sometimes these noises can even completely mask the signals. In the next section, we discuss in detail the noises generated in RTM using equation 2, and then we propose a new imaging condition to remove them in a subsequent section.

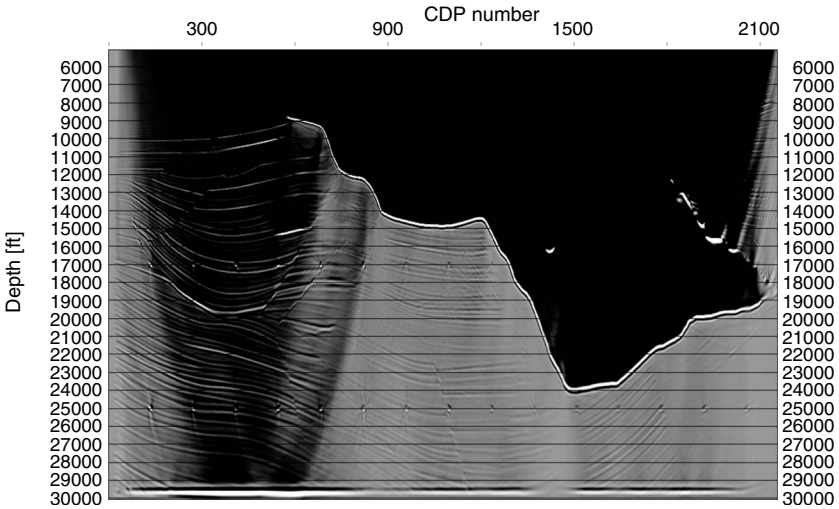


Figure 2. Reverse-time migration of the entire 2D line of the Sigsbee model using the crosscorrelation imaging condition in equation 2.

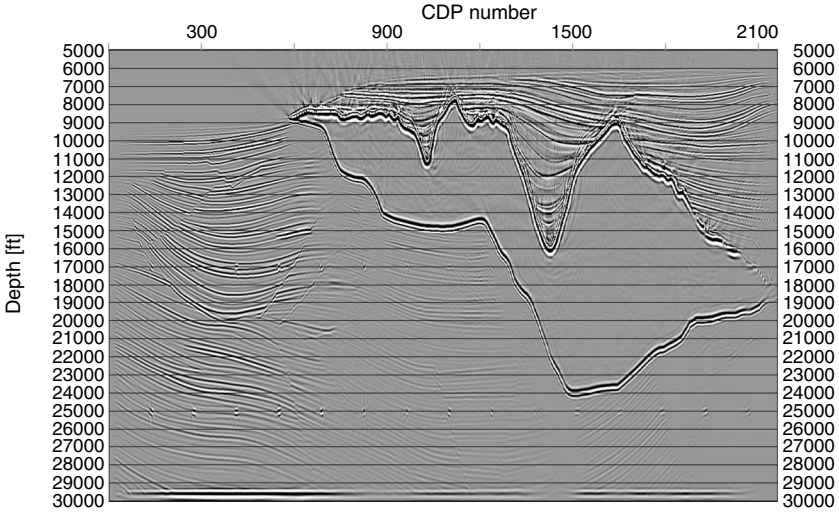


Figure 3. Band-pass filtered result of the image in Figure 2.

## NOISES IN REVERSE-TIME MIGRATION

The superiority of reverse-time migration over other imaging algorithms results from the fact that it utilizes the full acoustic wave equation to extrapolate the wavefields. Because this wave equation can accurately simulate wave propagation in all directions, including reflections and transmissions, the resulting imaging algorithm does not suffer from dip limitation and it can even image overturned beds and prismatic waves.

However, the same capability that lets RTM image structures illuminated by waves that turn past the horizontal direction also causes significant artifacts in the image when using the simple source and receiver crosscorrelation imaging condition in equation 2. Those artifacts are most serious along wave paths reflected from a hard interface in a velocity model. Figure 1a shows the RTM of one shot gather of the 2D synthetic Sigsbee data set using the imaging condition in equation 2, whereas Figure 2 is the RTM of the entire line. Clearly the large-amplitude, low-frequency noises seriously contaminate the image, and they make the shallow structures above the salt body completely invisible. Although those noises appear to have much lower frequency than the signals, simple band-pass filtering fails to remove their imprint completely as we can see in Figure 1b and Figure 3, which are the band-pass filtered version of Figure 1a and Figure 2, respectively. This type of noise is unique to RTM: It does not exist in one-way wave equation-based migration images constructed using the same crosscorrelation imaging condition.

To understand how those low-frequency noises are generated in a RTM image, we consider the wave paths in Figure 4 that come from a source located on the surface. As the wavefield propagates downward starting at a source location, the energy is partitioned into two parts when it encounters an interface: One part transmits through the interface and continues to propagate, whereas the other part is reflected back. The full acoustic wave equation is capable of properly propagating the reflected and transmitted energy. These wave paths are labeled as ***I*** (incident wave), ***T*** (transmitted wave), and ***R*** (reflected wave), respectively, in Figure 4. However, the receiver wavefield recorded in a seismic survey has gone through exactly the same interaction within the earth. In other words, in RTM, the simulated source and the recorded receiver wavefields have exactly the same propagation paths along which their energy correlate. The crosscorrelation of these two wavefields will not only produce amplitude at a reflector, but also at all nonreflecting points along the entire wave path, which builds up the low-frequency artifacts when the integration over time is applied.

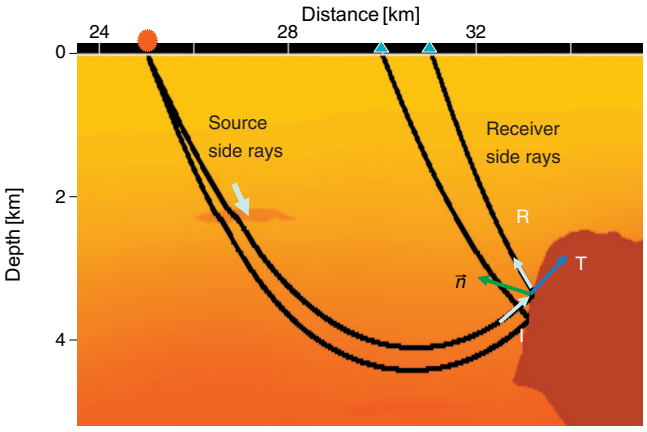


Figure 4. Some wave paths of the wavefield for a single point source.

In the following section, we propose a new imaging condition aimed at removing these noises for RTM. It distinguishes reflecting points from nonreflecting ones along a wave path, and the image is constructed only at reflecting points.

## A NEW IMAGING CONDITION FOR REVERSE-TIME MIGRATION

It is important to notice that, along a wave path, the source and receiver wavefields propagate always in the same direction unless it is at a reflecting point on an interface where reflections occur and the reflected wavefield propagates in different direction from the incident source wavefield with respect to the normal of the interface (vector $\vec{n}$ in Figure 4); that is, the projections of the incident and reflected waves on the reflector normal have opposite directions. Therefore, correlation of the decomposed source and receiver wavefields that have opposite propagation directions with respect to the normal will only create images at a reflector; no image will be constructed at nonreflecting points because at least one of the two wavefield components will be zero.

Without loss of generality, we consider a flat horizontal reflector in which the incident and reflected wavefields are therefore downgoing or upgoing, respectively. In RTM, the source and receiver wavefields extrapolated using the full acoustic wave equation contain both components, which can be partitioned mathematically as

$$s(t,\vec{x}) = s_d(t,\vec{x}) + s_u(t,\vec{x}) \tag{3}$$

and

$$r(t,\vec{x}) = r_d(t,\vec{x}) + r_u(t,\vec{x}), \tag{4}$$

where $s_d(t,\vec{x}), s_u(t,\vec{x})$ and $r_d(t,\vec{x}), r_u(t,\vec{x})$ are the downgoing and upgoing source and receiver wave components, respectively. Substituting equations 3 and 4 to equation 2, we get

$$\begin{aligned} I(\vec{x}) = &\int_0^{T_{\max}} s_d(t,\vec{x}) r_u(t,\vec{x}) dt + \int_0^{T_{\max}} s_u(t,\vec{x}) r_d(t,\vec{x}) dt \\ &+ \int_0^{T_{\max}} s_d(t,\vec{x}) r_d(t,\vec{x}) dt + \int_0^{T_{\max}} s_u(t,\vec{x}) r_u(t,\vec{x}) dt \\ = &\, I_{z1}(\vec{x}) + I_{z2}(\vec{x}) + I_{z3}(\vec{x}) + I_{z4}(\vec{x}). \end{aligned} \tag{5}$$

By definition, $I_{z1}$ is the crosscorrelation of the downgoing source and upgoing receiver wavefields; clearly, this is exactly what one will get in a one-way wave-equation migration. $I_{z2}$ is the crosscorrelation of the upgoing source and downgoing receiver wavefields. Figure 5 shows the raypath of a prismatic wave computed through raytracing, in which, at point A, the incident wave is downgoing, and the reflected wave propagates upward. On the other hand, at point B the upgoing wave is the incident wave and the reflected wave is downgoing. Therefore, such a trace can only be properly imaged when both reflections are taken into account, which requires the two terms $I_{z1}$ and $I_{z2}$ together.

The remaining two terms in equation 5 generate the noises seen in Figure 1, which are the crosscorrelation of the two wavefields that propagate in the same direction downgoing ($I_{z3}$) or upgoing ($I_{z4}$).

They correlate along the entire raypath and build up the low-frequency noise. An effective imaging condition can thus be formulated by keeping only the first two terms and excluding the other two as

$$I_{ud}(\vec{x}) = \int_0^{T_{\max}} [s_d(t,\vec{x})r_u(t,\vec{x}) + s_u(t,\vec{x})r_d(t,\vec{x})]dt. \quad (6)$$

The imaging condition proposed here is effective provided that the source and receiver wavefields are successfully decomposed into their upgoing and downgoing components. However, in some cases these wavefields may not be distinguishable in the upgoing and downgoing directions, as shown in Figure 4, because both the incident and reflected waves are upgoing, but they propagate horizontally in opposite directions. Thus, a similar partition of the wavefields in the horizontal direction may be needed in the imaging condition.

Mathematically, there are many methods that can be applied to decompose the source and receiver wavefields. In this paper, we propose a simple and effective approach using the Hilbert transform.

## WAVEFIELD DECOMPOSITION

To apply the proposed imaging condition in equation 6, the extrapolated source and receiver wavefields need to be decomposed into components for which the propagations can be projected to the same directions. For simplicity, we demonstrate the wavefield decomposition at a reflector having a vertical normal (i.e., a flat horizontal reflector) in which the decomposed wavefields will be upgoing or downgoing. In equations 3 and 4, the up-down decomposition is required at each subsurface location where the evolution of the wavefield with time simulates a vertical seismic profiling (VSP) data structure, as shown in Figure 6a. The upgoing and downgoing wave components are easily separable and can be simply computed in the $f$-$k$ domain as follows (Hu and McMechan, 1987):

$$S_D(\omega,k_z) = \begin{cases} S(\omega,k_z), & if\ \omega k_z \geq 0 \\ 0, & if\ \omega k_z < 0 \end{cases}, \quad (7)$$

$$S_U(\omega,k_z) = \begin{cases} S(\omega,k_z), & if\ \omega k_z < 0 \\ 0, & if\ \omega k_z \geq 0 \end{cases},$$

where $S(\omega,k_z)$ is the 2D Fourier transform of the source wavefield $s(t,z)$ at surface location $\vec{x}_s = (x,y)$ (i.e., $s(t,z) = s(t,x,y,z)$), and angular frequency $\omega$ and $S_{U,D}(\omega,k_z)$ are the decomposed upgoing and downgoing components in the $f$-$k_z$ domain, respectively. The required wavefields in equation 3 and 4 are obtained after 2D inverse Fourier transform to these two wavefield components. Similarly, the wavefield decomposition along the horizontal direction requires the operation at each constant depth slice as shown in Figure 6b, and the wavefield separation can be performed in the $f$-$k_x$ domain.

However, application of equation 7 requires 2D Fourier transforms along $t$ and $z$ dimensions for each surface location. This requires the wavefields at all time steps to be available, which is computationally expensive because of the large amount of data in a 3D problem.

Note that equation 6 only requires that the two correlating wavefield components propagate in different directions at each time. Based upon this observation, we propose an alternative to equation 6 that will produce the same result but is numerically much more efficient. Here, we define the new decomposed wavefields as

$$S_+(t,k_z) = \begin{cases} \bar{S}(t,k_z), & if\ k_z \geq 0 \\ 0 & if\ k_z < 0 \end{cases}, \quad (8a)$$

$$S_-(t,k_z) = \begin{cases} 0, & if\ k_z \geq 0 \\ \bar{S}(t,k_z) & if\ k_z < 0 \end{cases}$$

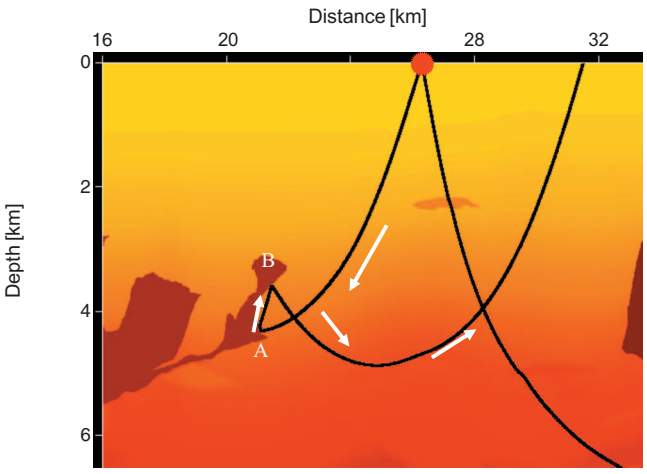


Figure 5. Wave path of prismatic waves.

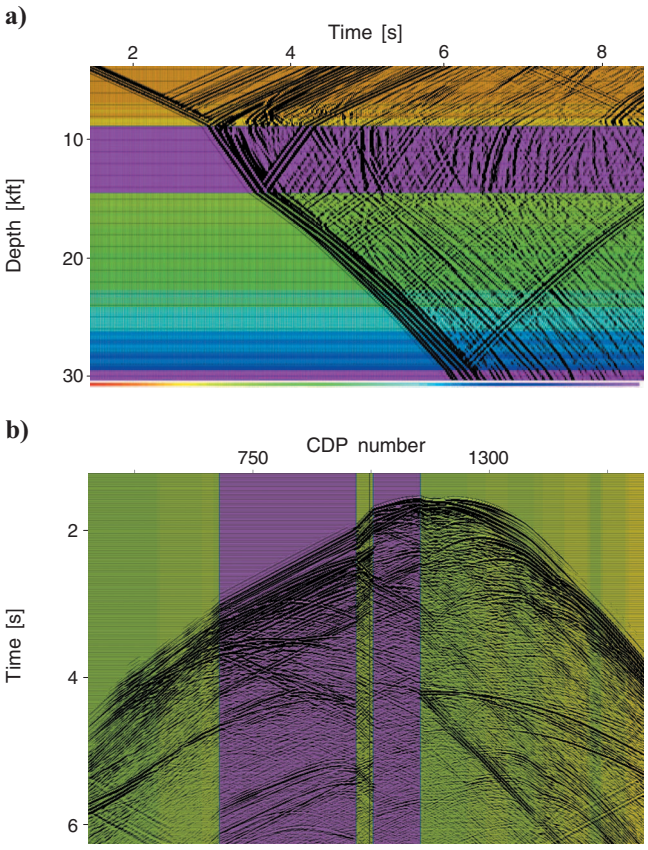


Figure 6. (a) A vertical section of the forward extrapolated source wavefield at a space location from the 2D Sigsbee model. (b) A horizontal slice of the forward extrapolated source wavefield at a constant depth from the 2D Sigsbee model.

and

$$R_+(t,k_z) = \begin{cases} \bar{R}(t,k_z), & if\ k_z \geq 0 \\ 0 & if\ k_z < 0 \end{cases}, \tag{8b}$$

$$R_-(t,k_z) = \begin{cases} 0, & if\ k_z \geq 0 \\ \bar{R}(t,k_z) & if\ k_z < 0 \end{cases},$$

where $\bar{S}(t,k_z)$ and $\bar{R}(t,k_z)$ are the 1D Fourier transform of the source wavefield $s(t,z)$ and receiver wavefield $r(t,z) = r(t,x,y,z)$ with respect to depth variable $z$. The imaging condition then needs to be adjusted as

$$I(\vec{x}) = \int_0^{T_{\max}} [s_+^*(t,\vec{x})r_-(t,\vec{x}) + s_-^*(t,\vec{x})r_+(t,\vec{x})]dt, \tag{9}$$

where $s_\pm(t,\vec{x})$ and $r_\pm(t,\vec{x})$ are the inverse Fourier transforms of $S_\pm(t,k_z)$ and $R_\pm(t,k_z)$ with $k_z$, respectively. The superscript "$*$" represents a complex conjugate because these functions are complex (see the Appendix for details).

It is straightforward to prove mathematically that equation 9 can be further simplified as follows because of the conjugate relationships between the two components of each wavefield:

$$I(\vec{x}) = 2\mathrm{Re}\left\{\int_0^{T_{\max}} [s_+(t,\vec{x})r_+(t,\vec{x})]dt\right\}. \tag{10}$$

As we can see in the Appendix, the new imaging result computed from equations 8a, 8b, 9, and 10 is equivalent to that computed using equations 6 and 7. In fact, equations 8a and 8b can be computed by the Hilbert transform of the wavefields along the $k_z$ direction. Figure 7 shows the RTM image of the 2D Sigsbee synthetic data using the imaging condition proposed here. By comparing with Figure 3, we see that the proposed imaging condition has successfully removed the high-amplitude, low-frequency noise.

## NUMERICAL EXAMPLES

We have applied the RTM using the proposed imaging condition to the well known 2D synthetic data set provided by BP (Billette and Brandsberg-Dahl, 2005). Because of its complicated structures as shown in the velocity model in Figure 8, this synthetic data set chal-

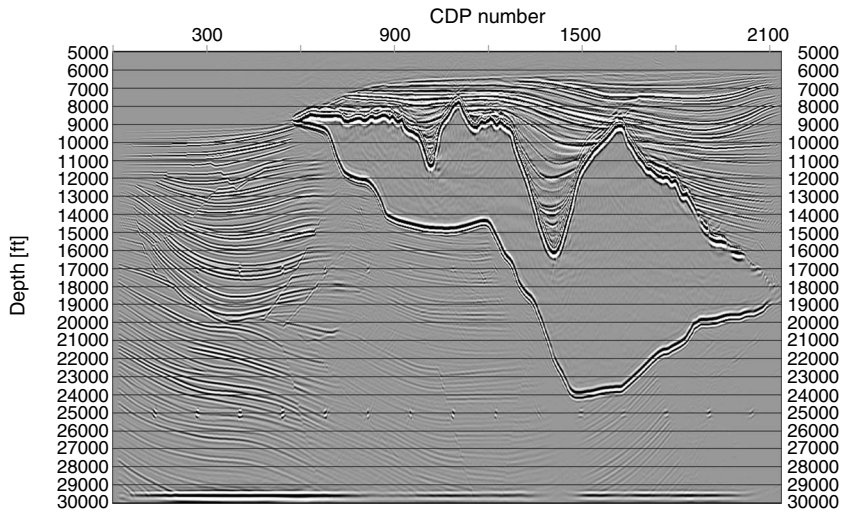


Figure 7. Reverse-time migration image (using the proposed imaging condition) of the Sigsbee model. This should be compared to Figure 2.

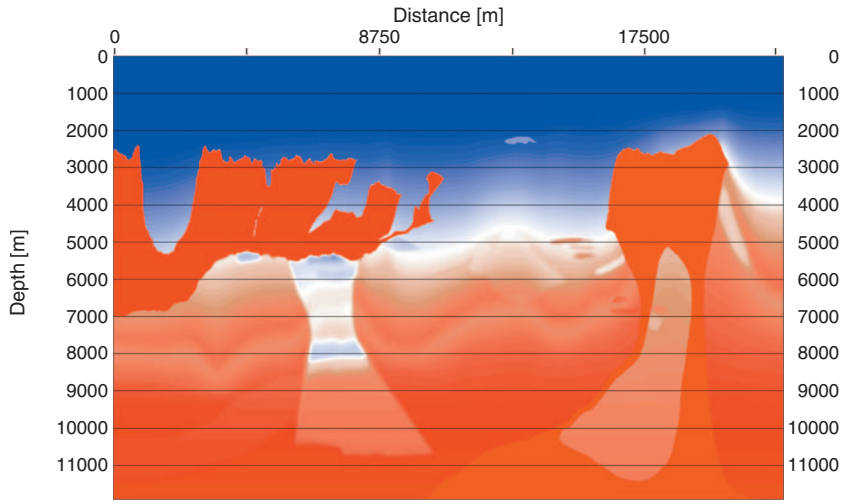


Figure 8. Velocity of the BP 2D synthetic model.

lenges imaging algorithms. Many structures, especially in the areas close to the two salt bodies, can only be imaged by an algorithm such as RTM that can properly handle overturned waves and complicated models. Figure 9 is the RTM image using the imaging condition in equation 10. It is clear that all of the steeply dipping structures are imaged very well, especially the salt flanks of the two salt bodies. The application of the proposed imaging condition properly images the complicated salt boundaries without producing noticeable artifacts. This can be seen more clearly in the zoomed images around the two salt bodies shown in Figure 10a and b, respectively.

Another example is from a 3D field data set. We migrated it using RTM with the proposed imaging condition. Figure 11a is one of the inline sections, whereas Figure 11b is one of its crossline sections. We see from these images that the imaging condition is capable of imaging the steeply dipping reflectors including overhangs (see Figure 11a); it does not produce the noise commonly seen even around a massive salt body (such as in Figure 11b).

Note that Figures 9 and 10 include the wavefield decomposition in vertical and horizontal directions, but the decomposition in the horizontal direction is only adaptively applied to the subsalt region; on the other hand, Figure 11 has the wavefield decomposed only in the vertical direction.

## DISCUSSION

The imaging condition defined in equation 10 works well in most cases. The successful applications of reverse-time migration to various data sets confirm that the proposed imaging condition is effective in removing the noises usually seen in a typical reverse-time migration image. However, there are certain cases in which the incident and reflected wavefields at an interface may not be distinguishable vertically or horizontally. For instance, at a dipping reflector of 60°, the reflection of a 75° angle incident wave (referring to the normal) will have the same direction as the incident wave in the horizontal and vertical directions (Figure 12). However, these two wavefield components always propagate in the opposite directions with respect to the normal direction. Thus, an imaging condition using the wavefield decomposition along the normal of an interface would be optimal. However, this requires local wavefield decomposition, which can be quite computationally intensive. A compromise would be to decompose the wavefields along some reference directions like the one that has 45° or 135° angles relative to the horizontal direction. Further investigation may be necessary to evaluate the applicability and value of these more general approaches.

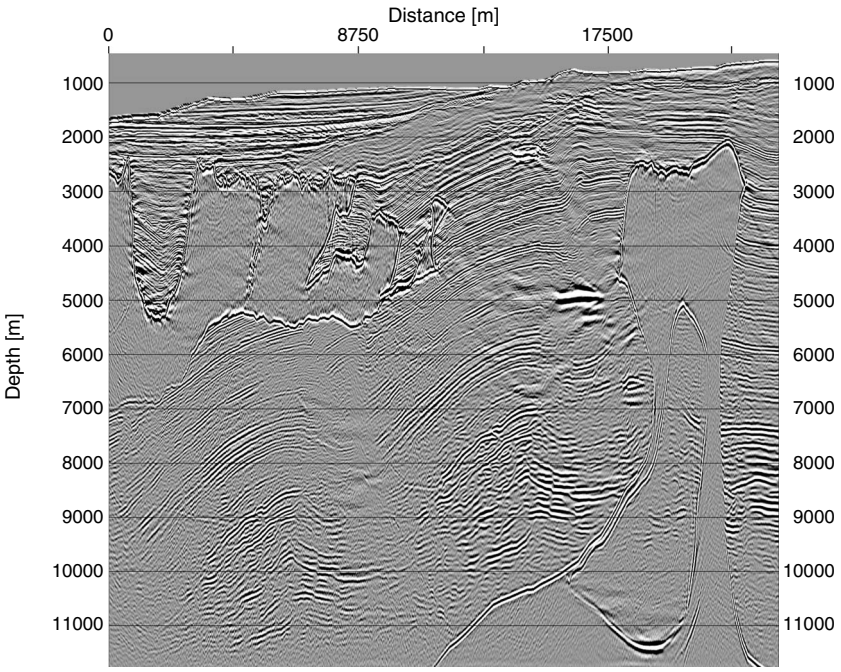


Figure 9. Reverse-time migration of the BP 2D synthetic model using the proposed imaging condition.

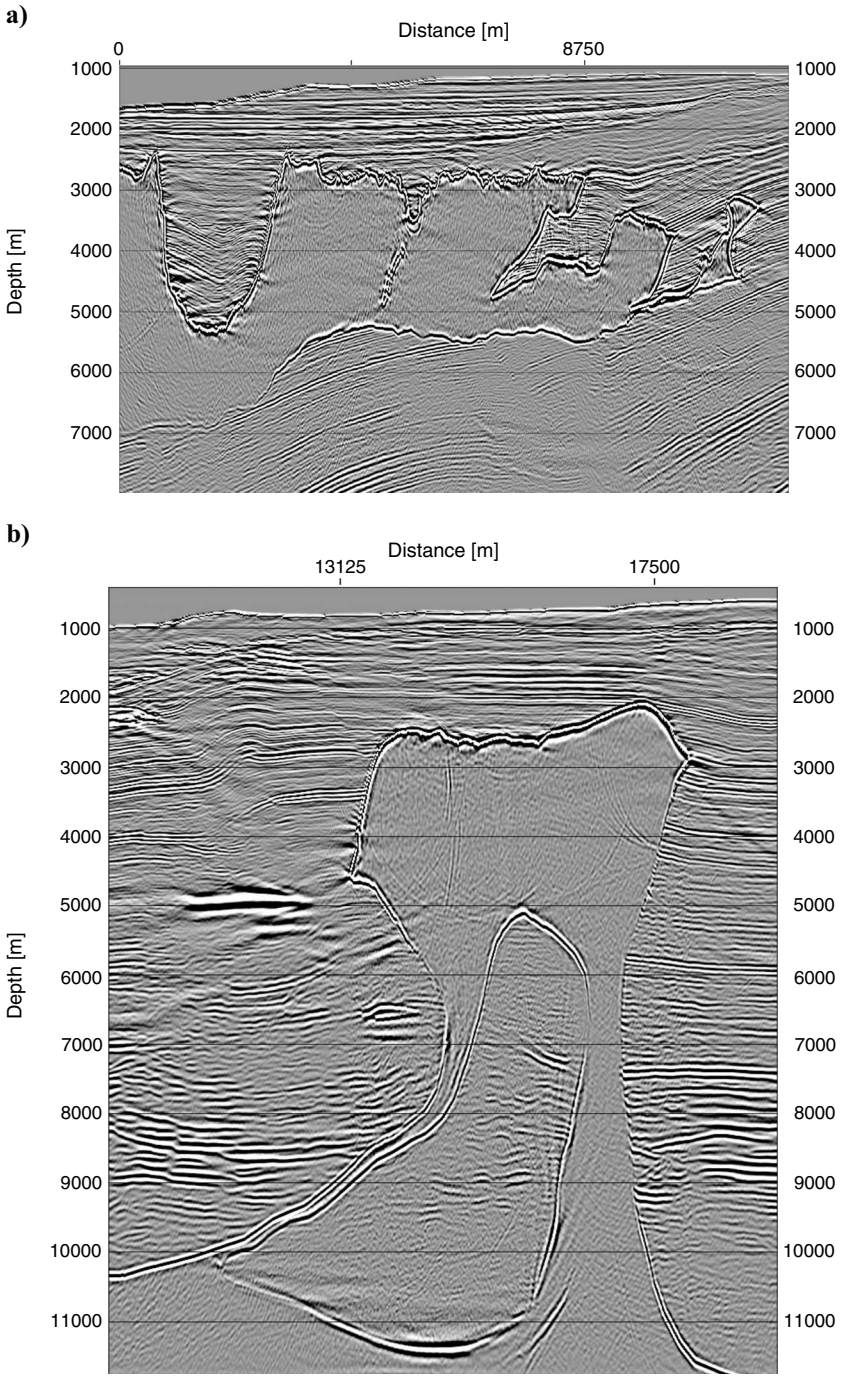


Figure 10. (a) The image around the left salt body for the RTM image of the BP 2D synthetic model using the proposed imaging condition. No artifact at the large contrast boundary like the salt interface is observed. (b) The image around the right salt body of the RTM image for the BP 2D synthetic model using the proposed imaging condition.

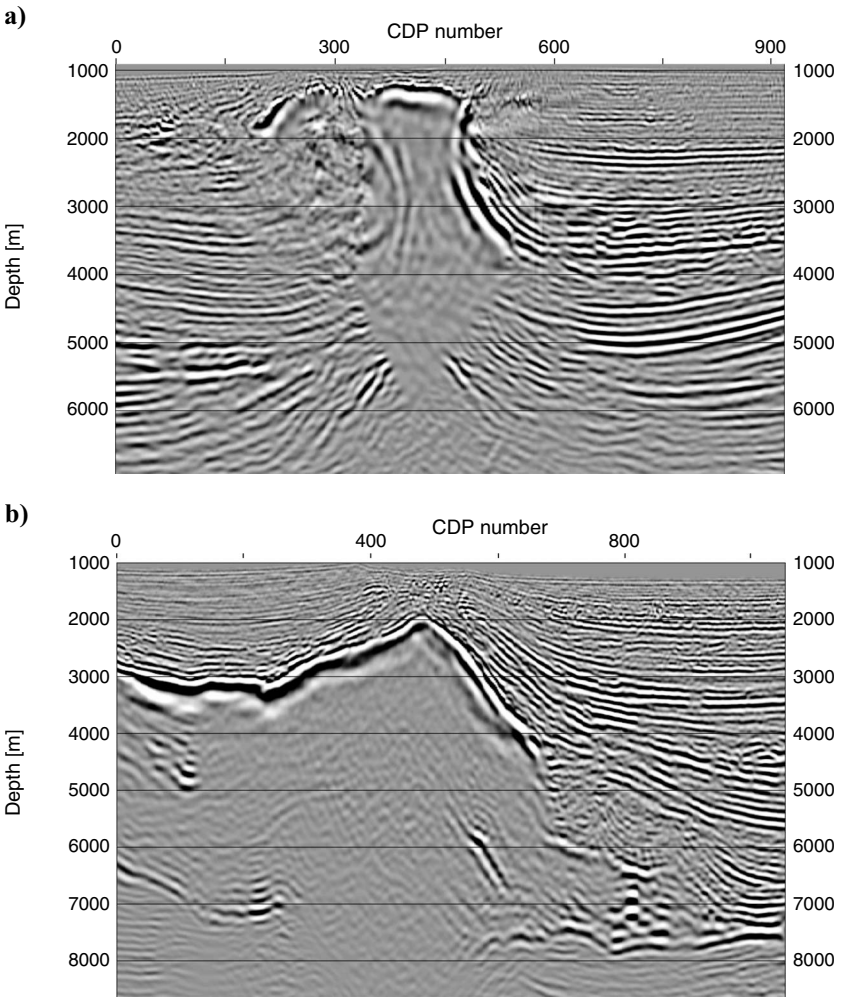


Figure 11. (a) One inline section out of a 3D RTM image of a 3D field data set using the proposed imaging condition. (b) One crossline section out of the same 3D RTM volume as in Figure 10a.

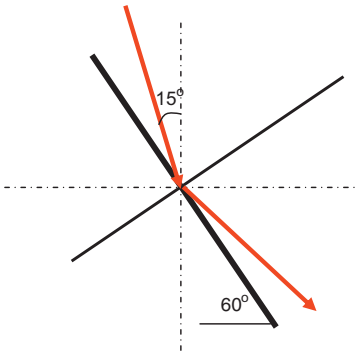


Figure 12. A diagram showing indistinguishable wavefields vertically and horizontally (see the main text for details).

## CONCLUSIONS

Reverse time migration can image steeply dipping reflectors and overturned waves because of its use of the acoustic wave equation in propagating the wavefields. However, this also causes the conventional correlation-based imaging condition to produce large-amplitude, low-frequency noises that contaminate the signals in the image. By decomposing the extrapolated wavefields and crosscorrelating them deterministically, the proposed new imaging condition in this paper successfully removes these artifacts from the images. Numerical tests have demonstrated its effectiveness. The proposed numerical scheme for wavefield decomposition significantly improves the efficiency of the imaging condition and only increases the overall computational cost by approximately 15% compared with the conventional crosscorrelation imaging condition; however, it can be a few times more expensive if the full $f - k$ wavefield decomposition is applied. This imaging condition is independent of the physical model used for the wavefield propagation and can be applied in isotropic and anisotropic reverse-time migration. In fact, it is also applicable to full elastic reverse-time migration.

## ACKNOWLEDGMENTS

We thank Hess Corporation for the permission to publish this paper. Faqi Liu and Scott A. Morton also thank Steve Checkles for his encouragement throughout the project and Xiaoguang Meng for his help on the real data example. We thank John Etgen, Mauricio Sacchi, Yu Zhang, and Mandy Wong for their valuable comments and suggestions. Finally, we thank BP for making the 2D synthetic model and data available.

## APPENDIX A

At a fixed surface location $(x,y)$, the 2D Fourier transform of the source wavefield $s(t,x,y,z)$ is

$$S(\omega,k_z)=\int_{-\infty}^{+\infty}\int_{-\infty}^{+\infty}s(t,z)e^{-i(t\omega+zk_z)}dtdz. \quad \text{(A-1)}$$

For simplicity, we omit the $x,y$ coordinates in the equations here; that is, we denote the wavefield $s(t,x,y,z)$ by $s(t,z)$.

In the Fourier domain, the upgoing and downgoing wavefield can be separated and formulated as

$$S_U(\omega,k_z)=\begin{cases}S(\omega,k_z), & if\ \omega k_z\geq 0\\ 0, & if\ \omega k_z<0\end{cases} \quad \text{(A-2a)}$$

and

$$S_D(\omega,k_z)=\begin{cases}S(\omega,k_z), & if\ \omega k_z<0\\ 0, & if\ \omega k_z\geq 0\end{cases}, \quad \text{(A-2b)}$$

where $S_U$ and $S_D$ are the Fourier transform of the decomposed upgoing and downgoing wave components, respectively. In the space-time domain, the two wavefields are

$$s_u(t,z)=\int_{-\infty}^{+\infty}\int_{-\infty}^{+\infty}S_U(\omega,k_z)e^{i(t\omega+zk_z)}d\omega dk_z \quad \text{(A-3a)}$$

and

$$s_d(t,z)=\int_{-\infty}^{+\infty}\int_{-\infty}^{+\infty}S_D(\omega,k_z)e^{i(t\omega+zk_z)}d\omega dk_z. \quad \text{(A-3b)}$$

Note that the wavefields defined in (A-3a and A-3b) are real functions.

Similarly, the decomposed receiver wavefield can also be formulated as

$$r_u(t,z)=\int_{-\infty}^{+\infty}\int_{-\infty}^{+\infty}R_U(\omega,k_z)e^{i(t\omega+zk_z)}d\omega dk_z \quad \text{(A-4a)}$$

and

$$r_d(t,z)=\int_{-\infty}^{+\infty}\int_{-\infty}^{+\infty}R_D(\omega,k_z)e^{i(t\omega+zk_z)}d\omega dk_z, \quad \text{(A-4b)}$$

where

$$R_U(\omega,k_z)=\begin{cases}R(\omega,k_z), & if\ \omega k_z\geq 0\\ 0, & if\ \omega k_z<0\end{cases} \quad \text{(A-5a)}$$

and

$$R_D(\omega,k_z)=\begin{cases}R(\omega,k_z), & if\ \omega k_z<0\\ 0, & if\ \omega k_z\geq 0\end{cases}, \quad \text{(A-5b)}$$

and $R(\omega,k_z)$ is the 2D Fourier transform of the receiver wavefield $r(t,z)=r(t,x,y,z)$.

With the above demonstration, the imaging condition in equation 6 can be represented in the time domain as

$$I(x,y,z)=\int[s_d(t,z)r_u(t,z)+r_d(t,z)s_u(t,z)]dt. \quad \text{(A-6)}$$

In the frequency domain, the correlation-based imaging condition can be presented in the following equation, as we have commonly seen in one-way wave-equation migration algorithms:

$$I(x,y,z)=\int[\bar{s}_d^{*}(\omega,z)\bar{r}_u(\omega,z)+\bar{s}_u^{*}(\omega,z)\bar{r}_d(\omega,z)]d\omega. \quad \text{(A-7)}$$

Here

$$\bar{s}_{u,d}(\omega,z)=\int_{-\infty}^{+\infty}s_{u,d}(t,z)e^{-it\omega}dt \quad \text{(A-8a)}$$

and

$$\bar{r}_{u,d}(\omega,z)=\int_{-\infty}^{+\infty}r_{u,d}(t,z)e^{-it\omega}dt. \quad \text{(A-8b)}$$

The superscript " $*$" represents the complex conjugate.

Now, we evaluate the wavefields defined in equation A-7 in the $f-k$ domain. For each angular frequency $\omega$,

$$S_+(\omega,k_z)=\begin{cases}S(\omega,k_z), & if\ k_z\geq 0\\ 0, & if\ k_z<0\end{cases} \quad \text{(A-9a)}$$

and

$$S_-(\omega,k_z)=\begin{cases}0, & if\ k_z\geq 0\\ S(\omega,k_z), & if\ k_z<0\end{cases} \quad \text{(A-9b)}$$

are the monofrequency components that always propagate in the opposite directions. To be more specific, when $\omega>0$, $S_+(\omega,k_z)$ contains all of the upgoing wave components whereas $S_-(\omega,k_z)$ defines all of the downgoing portion; however, when $\omega<0$, $S_+(\omega,k_z)$ becomes downgoing and $S_-(\omega,k_z)$ is upgoing. Therefore, $\bar{s}_\pm(\omega,z)=\int_{-\infty}^{+\infty}S_\pm(\omega,k_z)e^{izk_z}dk_z$ because the stack of the one-way propagating components are respectively still one-way propagating wave components.

In addition, from equations A-2a, A-2b, A-9a, and A-9b we can get the following equation:

$$S_U(\omega,k_z)=\begin{cases}S_+(\omega,k_z), & if\ \omega\geq 0\\ S_-(\omega,k_z), & if\ \omega<0\end{cases} \quad \text{(A-10a)}$$

and

$$S_D(\omega,k_z)=\begin{cases}S_-(\omega,k_z), & if\ \omega\geq 0\\ S_+(\omega,k_z), & if\ \omega<0\end{cases}. \quad \text{(A-10b)}$$

Therefore,

$$\bar{s}_u(\omega,z)=\begin{cases}\bar{s}_+(\omega,z), & if\ \omega\geq 0\\ \bar{s}_-(\omega,z), & if\ \omega<0\end{cases} \tag{A-11a}$$

and

$$\bar{s}_d(\omega,z)=\begin{cases}\bar{s}_-(\omega,z), & if\ \omega\geq 0\\ \bar{s}_+(\omega,z), & if\ \omega<0\end{cases}. \tag{A-11b}$$

Similarly, $\bar{r}_\pm(\omega,z)=\int_{-\infty}^{+\infty}R_\pm(\omega,k_z)e^{izk_z}dk_z$ respectively defines the one-way propagating receiver wavefield components, in which

$$R_+(\omega,k_z)=\begin{cases}R(\omega,k_z), & if\ k_z\geq 0\\ 0, & if\ k_z<0\end{cases} \tag{A-12a}$$

$$R_-(\omega,k_z)=\begin{cases}0, & if\ k_z\geq 0\\ R(\omega,k_z), & if\ k_z<0\end{cases}, \tag{A-12b}$$

$$\bar{r}_u(\omega,z)=\begin{cases}\bar{r}_+(\omega,z), & if\ \omega\geq 0\\ \bar{r}_-(\omega,z), & if\ \omega<0\end{cases}, \tag{A-13a}$$

and

$$\bar{r}_d(\omega,z)=\begin{cases}\bar{r}_-(\omega,z), & if\ \omega\geq 0\\ \bar{r}_+(\omega,z), & if\ \omega<0\end{cases}. \tag{A-13b}$$

Substituting equations in A-11a, A-11b, A-13a, and A-13b into equation A-7, we get

$$I(x,y,z)=\int[\bar{s}_+^*(\omega,z)\bar{r}_-(\omega,z)+\bar{s}_-^*(\omega,z)\bar{r}_+(\omega,z)]d\omega. \tag{A-14}$$

Therefore, we can get the new imaging condition in the time domain as

$$I(x,y,z)=\int[s_+^*(t,z)r_-(t,z)+s_-^*(t,z)r_+(t,z)]dt, \tag{A-15}$$

where

$$s_\pm(t,z)=\int_{-\infty}^{+\infty}\bar{s}_\pm(\omega,z)e^{i\omega t}d\omega \tag{A-16a}$$

and

$$r_\pm(t,z)=\int_{-\infty}^{+\infty}\bar{r}_\pm(\omega,z)e^{i\omega t}d\omega. \tag{A-16b}$$

Note here that these fields are no longer real functions.

From the equations in A-9a, A-9b, A-11a, A-11b, A-13a, and A-13b, we can say that the equations in A-16a and A-16b are the Hilbert transform of the source and receiver wavefields in the depth dimension, respectively.

## REFERENCES


Baysal, E., D. D. Kosloff, and J. W. C. Sherwood, 1983, Reverse-time migration: Geophysics, **48**, 1514–1524, doi: 10.1190/1.1441434.

Baysal, E., D. D. Kosloff, and J. W. C. Sherwood, 1984, A two-way nonreflecting wave equation: Geophysics, **49**, 132–141, doi: 10.1190/1.1441644.

Billette, F. J., and S. Brandsberg-Dahl, 2005, The 2004 BP velocity benchmark: Presented at the 67th Annual International Conference and Exhibition, EAGE, Extended Abstracts, B035.

Claerbout, J. F., 1985, Imaging the earth's interior: Blackwell Science Inc.

Dussaud, E., W. W. Symmes, P. Williamson, L. Lemaistre, and P. Singer, 2008, Computational strategies for reverse-time migration: 78th Annual International Meeting, SEG, Expanded Abstracts, 2267–2271.

Etgen, J., S. H. Gray, and Y. Zhang, 2009, An overview of depth imaging in exploration geophysics: Geophysics, **74**, no. 6, WCA5–WCA17, doi: 10.1190/1.3223188.

Fletcher, R. F., P. Fowler, P. Kitchenside, and U. Albertin, 2005, Suppressing artifacts in prestack reverse-time migration: 75th Annual International Meeting, SEG, Expanded Abstracts, 2049–2051.

Guitton, A., B. Kaelin, and B. Biondi, 2006, Least-square attenuation of reverse-time migration artifacts: 76th Annual International Meeting, SEG, Expanded Abstracts, 2348–2352.

Hu, L., and G. A. McMechan, 1987, Wave-field transformations of vertical seismic profiles: Geophysics, **52**, 307–321, doi: 10.1190/1.1442305.

Liu, F., G. Zhang, S. A. Morton, and J. P. Leveille, 2007, Reverse-time migration using one-way wavefield imaging condition: 77th Annual International Meeting, SEG, Expanded Abstracts, 2170–2174.

Loewenthal, D., and I. R. Mufti, 1983, Reverse-time migration in spatial frequency domain: Geophysics, **48**, 627–635, , doi: 10.1190/1.1441493.

Loewenthal, D., P. A. Stoffa, and E. L. Faria, 1987, Suppressing the unwanted reflections of the full wave equation: Geophysics, **52**, 1007–1012, doi: 10.1190/1.1442352.

McMechan, G. A., 1983, Migration by extrapolation of time-dependent boundary values: Geophysical Prospecting, **31**, 413–420, doi: 10.1111/j.1365-2478.1983.tb01060.x.

Symes, W., 2007, Reverse-time migration with optimal check pointing: Geophysics, **72**, no. 5, SM213–SM221, doi: 10.1190/1.2742686.

Whitmore, D. N., 1983, Iterative depth imaging by back time propagation: 53rd Annual International Meeting, SEG, Expanded Abstracts, 382–385.

Yoon, K., and K. J. Marfurt, 2006, Reverse-time migration using the pointing vector: Exploration Geophysics, **37**, 102–107, doi: 10.1071/EG06102.

Zhang, Y., and J. Sun, 2009, Practical issues in reverse-time migration: True amplitude gathers, noise removal and harmonic-source encoding: First Break, **26**, 19–25.